


Article

# Zr(OH)<sub>4</sub>/GO Nanocomposite for the Degradation of Nerve Agent Soman (GD) in High-Humidity Environments

Seongon Jang <sup>†</sup>, Dongwon Ka <sup>†</sup>, Hyunsook Jung, Min-Kun Kim, Heesoo Jung and Youngho Jin \* 

4th R&D Institute-6th Directorate Agency for Defense Development, Daejeon 34186, Korea; ondol0809@gmail.com (S.J.); rkehd47@gmail.com (D.K.); junghs@add.re.kr (H.J.); mkkim@add.re.kr (M.-K.K.); hsjung@add.re.kr (H.J.)

\* Correspondence: cadetnet@add.re.kr; Tel.: +82-42-821-2203; Fax: +82-42-823-3400

<sup>†</sup> Authors contributed equally.

Received: 28 April 2020; Accepted: 29 June 2020; Published: 1 July 2020



**Abstract:** Zirconium hydroxide, Zr(OH)<sub>4</sub> is known to be highly effective for the degradation of chemical nerve agents. Due to the strong interaction force between Zr(OH)<sub>4</sub> and the adsorbed water, however, Zr(OH)<sub>4</sub> rapidly loses its activity for nerve agents under high-humidity environments, limiting real-world applications. Here, we report a nanocomposite material of Zr(OH)<sub>4</sub> and graphene oxide (GO) which showed enhanced stability in humid environments. Zr(OH)<sub>4</sub>/GO nanocomposite was prepared via a dropwise method, resulting in a well-dispersed and embedded GO in Zr(OH)<sub>4</sub> nanocomposite. The nitrogen (N<sub>2</sub>) isotherm analysis showed that the pore structure of Zr(OH)<sub>4</sub>/GO nanocomposite is heterogeneous, and its meso-porosity increased from 0.050 to 0.251 cm<sup>3</sup>/g, compared with pristine Zr(OH)<sub>4</sub> prepared. Notably, the composite material showed a better performance for nerve agent soman (GD) degradation hydrolysis under high-humidity air conditions (80% relative humidity) and even in aqueous solution. The soman (GD) degradation by the nanocomposite follows the catalytic reaction with a first-order half-life of 60 min. Water adsorption isotherm analysis and diffuse reflectance infrared Fourier transform (DRIFT) spectra provide direct evidence that the interaction between Zr(OH)<sub>4</sub> and the adsorbed water is reduced in Zr(OH)<sub>4</sub>/GO nanocomposite, indicating that the active sites of Zr(OH)<sub>4</sub> for the soman (GD) degradation, such as surface hydroxyl groups are almost available even in high-humidity environments.

**Keywords:** Zr(OH)<sub>4</sub>/GO nanocomposite; graphene oxide; degradation; nerve agent; soman (GD); humidity

## 1. Introduction

Chemical warfare nerve agents including soman (GD) (*O*-pinacolyl methylphosphonofluoridate) are known to be the most lethal among chemical warfare agents (CWAs), have been often used in combat zones as tactical weapons and for terrorism during recent decades [1]. In particular, nerve agents have not only fatal effects in acute phase of poisoning but also considerable long-term complications due to irreversible inhibition of acetylcholine esterase [2]. Although all CWAs are banned by the Chemical Weapons Convention (CWC), several countries are still stockpiling chemical agents [3]. Therefore, effective degradation methods must be prepared in order to protect any important equipment, facilities, and environments from the toxic chemical agents [4,5].

Novel materials making nerve agents decompose into less or nontoxic molecules have been going through noticeable evolutions in recent years [6–9]. Metal-organic frameworks (MOFs) [10], metal oxides (hydroxides) [11,12], and composite materials [12] have attracted significant attention

as potential materials [13–16]. Zirconium hydroxide ( $\text{Zr}(\text{OH})_4$ ), which has various surface hydroxyl species and defect sites, is considered as one of the most prominent materials because of its superior sorptive property and wide range of reactivity toward nerve agents [17–22]. However, many existing researches on  $\text{Zr}(\text{OH})_4$  studied its effects on simulants, rather than real CWAs [17,20–24]. Furthermore, it is not clearly known how real atmospheric conditions affect its CWAs degradation performance in real-operational field. Many metal oxides and hydroxides are very sensitive to  $\text{H}_2\text{O}$  and  $\text{CO}_2$  and form byproducts that may block their reactive sites. It is already known that water molecules form additional interfaces on the surface and significantly affect the surface reaction chemistry of metal oxides and hydroxides [25].

Graphene oxide (GO), as a derivative of graphene, has a unique 2D lamellar structure and many attractive properties [26]. There are abundant oxygenated functional groups including hydroxyl, epoxy, carboxyl, and carbonyl groups on GO surface, which can bind with the metallic centers of the metal oxides, metal hydroxides, or MOFs. These functional groups can be served as activation sites for the crystal growth onto the surface of GO [27,28]. Moreover, it was previously reported that the GO can improve the catalytic activity by inducing a synergistic effect between components in the composites [29,30].

It is known that the GO addition can increase the surface area in the composites with  $\text{Zr}(\text{OH})_4$  due to new pores at the interface of both components in  $\text{Zr}(\text{OH})_4/\text{GO}$  nanocomposite [20]. Here, we supposed that GO would improve availability of the active sites for reactants to access. In order to benefit from the advantages of both  $\text{Zr}(\text{OH})_4$  and GO, we attempted to synthesize  $\text{Zr}(\text{OH})_4/\text{GO}$  nanocomposite and pristine  $\text{Zr}(\text{OH})_4$  and identify their degradation abilities toward soman (GD) after exposure to high-humidity air conditions.  $\text{Zr}(\text{OH})_4/\text{GO}$  nanocomposite and pristine  $\text{Zr}(\text{OH})_4$  were prepared by a dropwise method which is useful to control the rate of precipitation. The degradation of soman (GD) was investigated with the materials after exposure at 80% relative humidity (RH) for various times. The time course of the reactions was studied by phosphorus-31 solid state-magic angle spinning nuclear magnetic resonance ( $^{31}\text{P}$  SS-MAS NMR). Water isotherms and DRIFT analysis were additionally performed to identify the reason for the better ability of  $\text{Zr}(\text{OH})_4/\text{GO}$  nanocomposite to degrade the soman (GD) agent in high-humidity environments.

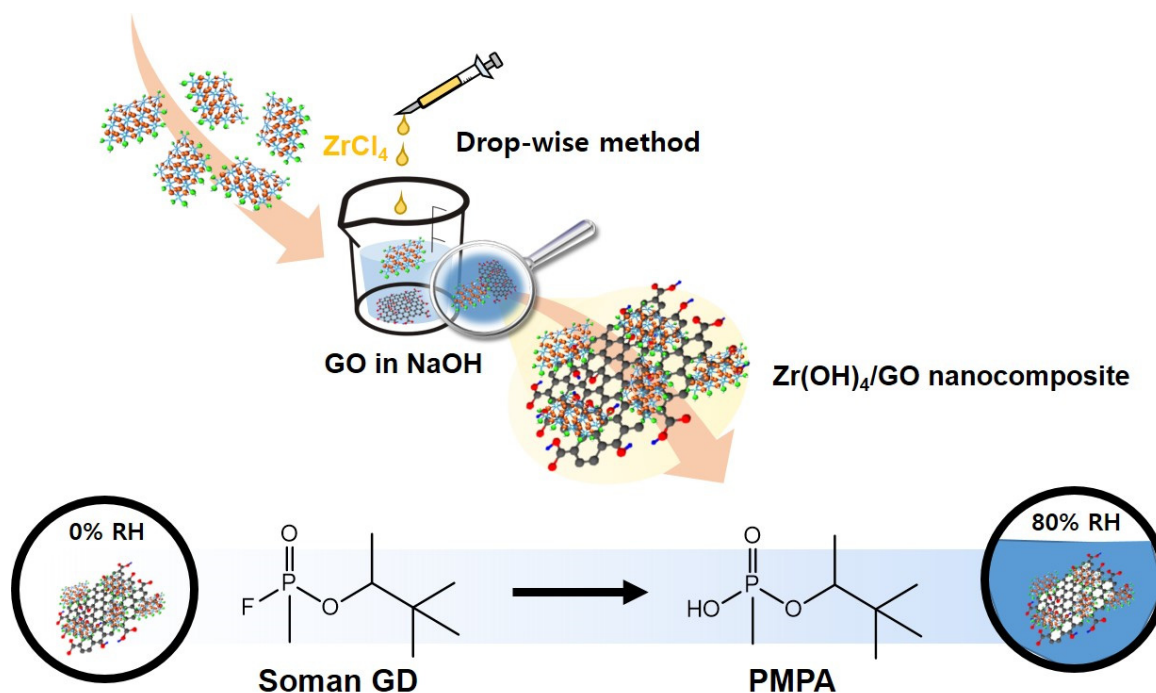
## 2. Materials and Methods

### 2.1. Materials

Graphene oxide (GO), zirconium chloride ( $\text{ZrCl}_4 \geq 99.5\%$ , powder), and sodium hydroxide ( $\text{NaOH}$ —reagent grade  $\geq 98.0$  pellets anhydrous) were purchased from Sigma-Aldrich (Seoul, Korea) and used without any pre-treatment. The soman (GD) agent was synthesized at the Organisation for the Prohibition of Chemical Weapons (OPCW) designated laboratories. The purity of the agent was determined by gas chromatography-mass spectrometry (GC-MS) and hydrogen-1 nuclear magnetic resonance ( $^1\text{H}$  NMR) and exceeded 99%.

### 2.2. Preparation of $\text{Zr}(\text{OH})_4/\text{GO}$ Nanocomposite and $\text{Zr}(\text{OH})_4$

$\text{NaOH}$  (0.05 M) and  $\text{ZrCl}_4$  (0.05 M) were added into separate containers filled with deionized (DI) water and sonicated for 30 min. GO powder (5 wt % of the final mass of the composite) was dispersed in 1 L of  $\text{NaOH}$  solution through ultra-sonication for 30 min. A stoichiometric amount of  $\text{ZrCl}_4$  (0.25 L, 0.05 M) solution was dropwise added into the solution at a constant rate (0.75 mL/min) as illustrated in Scheme 1. The suspension was stirred vigorously for 5 h to obtain the precipitate of  $\text{Zr}(\text{OH})_4/\text{GO}$  nanocomposite. The obtained precipitate was washed several times with deionized water by using a centrifuge at 6000 rpm for 15 min until its pH became nearly neutral (pH 7–8). Finally, it was dried at 60 °C in vacuum oven for 48 h. Pristine  $\text{Zr}(\text{OH})_4$  was synthesized in a manner similar to  $\text{Zr}(\text{OH})_4/\text{GO}$  nanocomposite without the addition of GO.



**Scheme 1.** Degradation of nerve agent soman (GD) by Zr(OH)<sub>4</sub>/GO nanocomposite in a high-humidity environment.

### 2.3. Characterization

The structures and properties of Zr(OH)<sub>4</sub> and Zr(OH)<sub>4</sub>/GO nanocomposite materials were characterized by various methods: scanning electron microscopy (SEM) with energy dispersive spectroscopy (EDS), X-ray diffraction (XRD), thermogravimetric analysis (TGA), nitrogen adsorption-desorption isotherms, water vapor adsorption isotherms, and diffuse reflectance infrared Fourier transform spectroscopy (DRIFT).

SEM and EDS were used to analyze the surface morphology and composition of the samples, respectively. The instrument used was a Quanta 650 SEM (FEI, Hillsboro, OR, USA) equipped with EDS detector (X1 Analyzer, EDAX, Berwyn, IL, USA). The materials were coated with gold using a Sputter Coater 108 (Cressington, Oxhey, UK) prior to the SEM observations. The measurements were performed with acceleration voltages ranging from 5 to 15 kV. EDS spectra directly revealed the presence of the atomic elements (Carbon, Oxygen, and Zirconium) in the sample. XRD patterns were obtained using a powder X-ray diffractometer (AXS GmbH, Bruker, Madison, WI, USA), which used CuK $\alpha$  radiation (operated at 40 kV and 40 mA). The diffraction patterns were collected with a 2 $\theta$  scan from 10° to 70°. TGA measurements were performed to study thermal stability using a thermogravimetric analyzer (TGA Q500, TA Instruments, New Castle, PA, USA). The heating rate was 5 °C/min and the total N<sub>2</sub> flow rate was 100 mL/min. The samples were heated up to 800 °C, starting from 30 °C. The nitrogen adsorption-desorption isotherms were obtained through an ASAP 2020 system (Micromeritics Instrument Corp., Norcross, GA, USA) at 77 K. The samples were degassed at 393 K under 133 mbar before the measurements. The isotherms were used to calculate the surface area,  $S_{\text{BET}}$  (BET method); the mesopore volume,  $V_{\text{meso}}$  (calculated by Barrett–Joyner–Halenda (BJH) method); and the total pore volume,  $V_{\text{t}}$  (calculated from the last point of the isotherm). To measure DRIFT, a Fourier-transform infrared (FTIR) spectrometer (Thermo Scientific, Nicolet i50, Swedesboro, NJ, USA) was used with the DiffusIR accessory (PIKE Technologies, Fitchburg, MA, USA). Before the measurement, the sample was purged with N<sub>2</sub> gas to reduce background noise. The spectra were collected 128 times, and the resolution was 0.482 cm<sup>-1</sup>.

#### 2.4. Degradation of Nerve Agent Soman (GD)

Disclaimer: Small doses of the nerve agent soman (GD) are known to be lethal if in contact with the skin or inhaled through the nose or mouth. Experiments should be performed only by trained personnel in adequate facilities.

Zr(OH)<sub>4</sub>/GO nanocomposite and Zr(OH)<sub>4</sub> (10 mg, each) in a 2 mL vial were investigated with exposure to 80% relative humidity (80% RH) condition at 25 °C for various hours (72, 168, and 324 h). Subsequently, 0.4 µL of soman (GD) was added with 20 µL of pentane in each vial containing materials [14]. The vials were agitated vigorously on a vortex mixer for 10 min. The residual GD was extracted with 1.5 mL of ethyl acetate (DAEJUNG, Daejeon, South Korea, Guaranteed Reagent ≥ 99.5%) for 2 h, and the solution was analyzed through GC-MS (MSD 5977A, Agilent Technology, Madison, WI, USA). The column mounted on the GC-MS system was 30 m in length and 250 µm in internal diameter, with a liquid-film thickness of 0.25 µm. The analysis was operated by increasing the temperature from 45 to 230 °C at a rate of 10 °C/min. The carrier gas was helium. The injection volume and total flow were 1 µL and 3 mL/min, respectively. There was no split during the measurement.

#### 2.5. Reaction Products Analysis

The degradation product, *O*-pinacolyl-methylphosphonic acid (PMPA) was confirmed by GC-MS (MSD 5977A, Agilent Technology). A portion of the supernatant solution in the glass vial were sampled 10 min after the reaction start, and the sample was sufficiently evaporated at 60 °C by N<sub>2</sub> blowing for 30 min. Prior to analysis, PMPA was derivatized with bis(trimethylsilyl)trifluoroacetamide (Sigma-aldrich, Seoul, Korea, for GC derivatization ≥ 99.0%) at 70 °C for 2 h [31,32]. GC-MS analysis showed the trimethylsilyl (TMS) derivative, PMPA-TMS.

#### 2.6. <sup>31</sup>P SS-MAS NMR Analysis

<sup>31</sup>P SS-MAS NMR spectra were obtained using an Oxford NMR instrument (AS600, Agilent Technologies, Santa Clara, CA, USA) equipped with a 4 mm probe using direct polarization, spinning rate of approximately 3000 Hz and a 90° pulse width of 4 µs. Zr(OH)<sub>4</sub>/GO nanocomposite and was packed in the zirconium oxide rotor (46 µL pore volume, Revolution NMR, LLC, Fort Collins, CO, USA) and spiked with 5 µL of soman (GD). The rotor was sealed with Kellogg and Fluoropolymer (Kel-F) caps (Revolution NMR, Fort Collins, CO, USA). The delay time between the pulses was 5 s. The <sup>31</sup>P SS-MAS NMR spectra were referenced to external phosphoric acid at 0 ppm.

### 3. Results and Discussion

#### 3.1. Characterization of Zr(OH)<sub>4</sub>/GO Nanocomposite and Pristine

Morphological features and chemical composition of as-synthesized Zr(OH)<sub>4</sub>/GO nanocomposite and pristine Zr(OH)<sub>4</sub> by dropwise method were characterized by using SEM images and EDS spectra. SEM images of Zr(OH)<sub>4</sub>/GO nanocomposite were taken in the backscatter mode in order to distinguish easily inorganic (Zr(OH)<sub>4</sub>, bright) and organic materials (GO, dark) through the brightness. As presented in Figure 1, many GO flakes were well-dispersed and embedded in Zr(OH)<sub>4</sub>/GO nanocomposite, while small Zr(OH)<sub>4</sub> particles agglomerated into large particles in pristine Zr(OH)<sub>4</sub>. This uniformity might be attributed to vigorous stirring during the precipitation and the excellent dispersability of GO in aqueous solution. The EDS spectra of Zr(OH)<sub>4</sub>/GO nanocomposite indicates not only that the product consists of C, O, and Zr (Figure S1) but also that GO flakes were successfully introduced on the surface of Zr(OH)<sub>4</sub>, not just physically mixed. The XRD patterns of Zr(OH)<sub>4</sub>/GO nanocomposite are similar to those of pristine Zr(OH)<sub>4</sub>, which suggests that there was no change in Zr(OH)<sub>4</sub> structure by forming nanocomposite with GO (Figure S2). Furthermore, both of materials have broad peaks because of their lack of crystallinity.

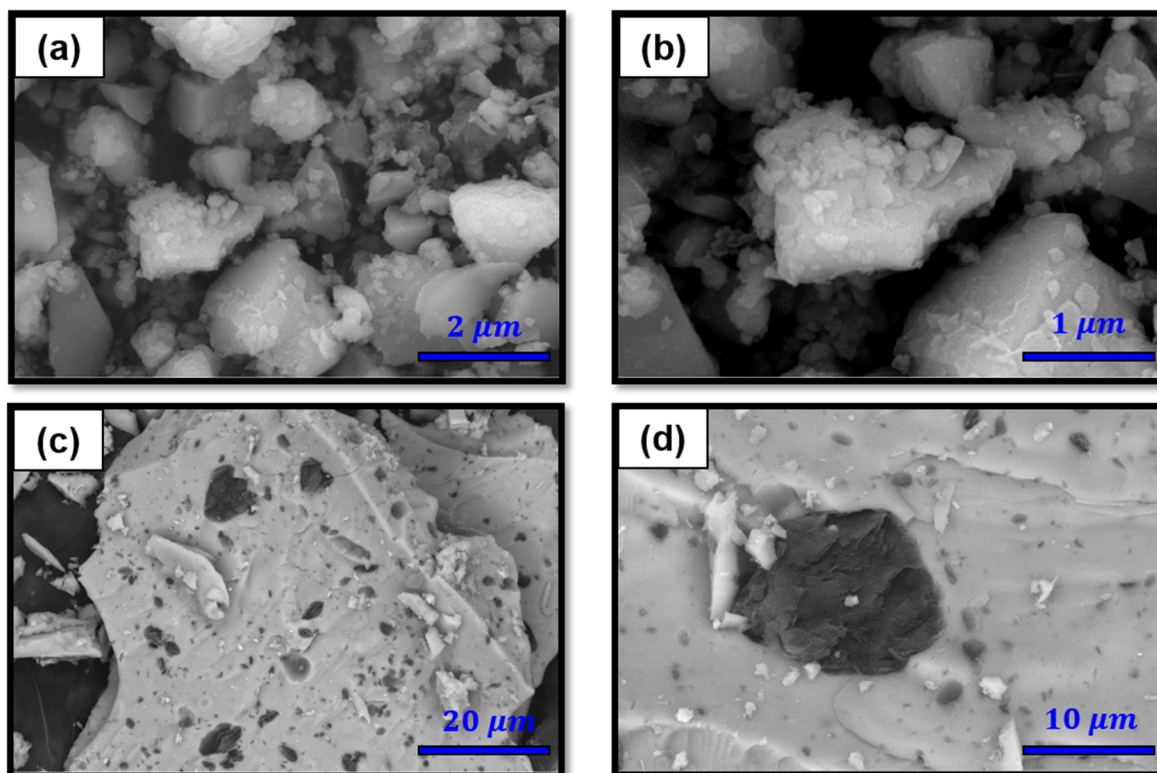


**Figure 1.** SEM images of  $Zr(OH)_4$  (a) in low and (b) in high magnification and  $Zr(OH)_4/GO$  nanocomposite (c) in low and (d) in high magnification. Images of  $Zr(OH)_4/GO$  nanocomposite were taken in the backscatter mode to distinguish GO from  $Zr(OH)_4$ .

The nitrogen adsorption-desorption isotherms at 77 K and pore size distribution for  $Zr(OH)_4/GO$  nanocomposite and pristine  $Zr(OH)_4$  are presented in Figure 2. The Brunauer–Emmett–Teller ( $S_{BET}$ ), total pore volumes ( $V_t$ ), and mesopore volumes ( $V_{meso}$ ) for  $Zr(OH)_4/GO$  nanocomposite and  $Zr(OH)_4$  are summarized in Table 1. The nitrogen adsorption–desorption isotherms (Figure 2a) of  $Zr(OH)_4/GO$  nanocomposite showed the higher amount of nitrogen adsorbed and discordance between the nitrogen adsorption and desorption, while pristine  $Zr(OH)_4$  exhibited typical type I isotherms, as reported in the literature [33]. Indeed,  $Zr(OH)_4/GO$  nanocomposite exhibits a type E hysteresis loop, which is typical characteristic of “ink-bottle” pores [34], corresponding to type IV. The hysteresis loop of  $Zr(OH)_4/GO$  nanocomposite at the relative pressure ( $p/p_0$ ) ranging from 0.45 to 0.75 indicates the possible presence of mesoporous structure [35]. The pore size distribution (Figure 2b) demonstrated that most of pores in  $Zr(OH)_4/GO$  nanocomposite were mesopores (2–50 nm in size). The BET surface area increased from 216 to 274  $m^2/g$ , respectively, in  $Zr(OH)_4/GO$  nanocomposite. It is noted that  $Zr(OH)_4/GO$  nanocomposite has a relatively larger surface area, higher pore volume, and looser structure than that of  $Zr(OH)_4$ . The average pore size also increased from 2–3.2 nm to 3.7 nm after addition of GO particles. These results demonstrate that uniformly embedded GO between  $Zr(OH)_4$  enhance the structural heterogeneity and porosity of the composite [20], which may improve the adsorption capability of  $Zr(OH)_4$  [36–38].

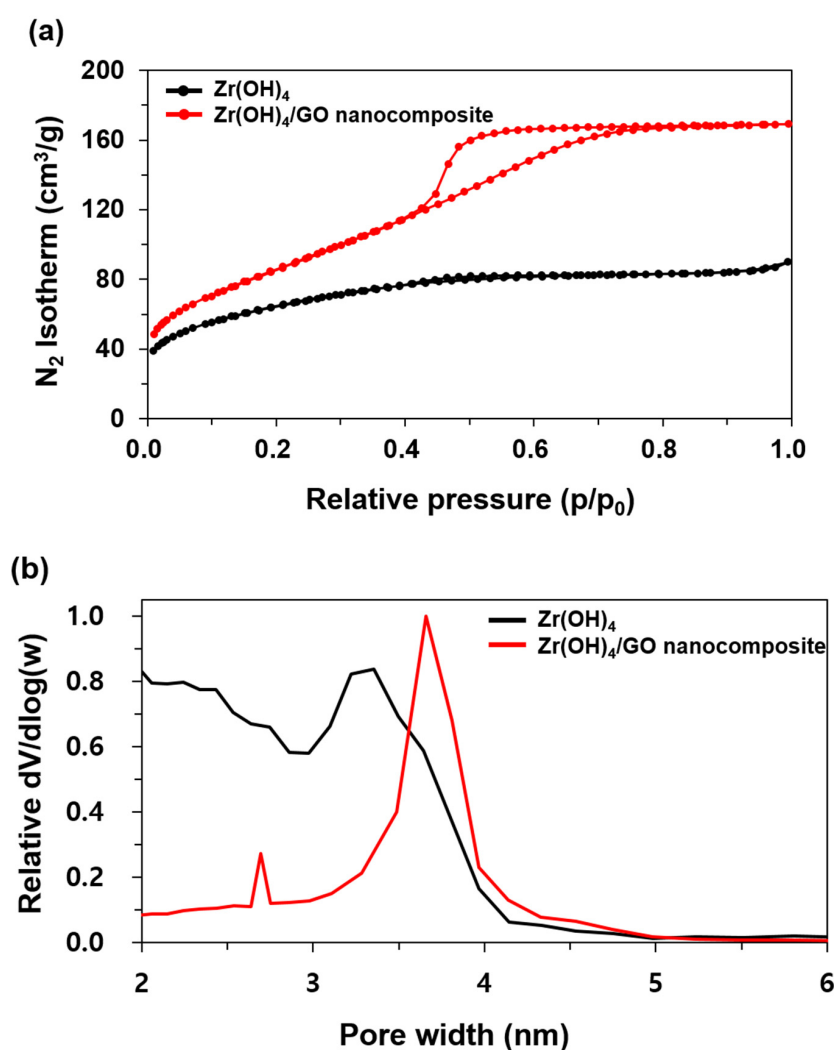


**Figure 2.** (a)  $N_2$  gas adsorption-desorption isotherms at 77 K and (b) pore size distribution for  $Zr(OH)_4$ /GO nanocomposite and pristine  $Zr(OH)_4$ . All samples were degassed at 393 K under 133 mbar before measurement to eliminate impurities in pores. Pore size distribution was analyzed by using the Barrett–Joyner–Halenda (BJH) method based on Kelvin equation.

**Table 1.** Characteristics of the porous structure of and  $Zr(OH)_4$ /GO nanocomposite and pristine  $Zr(OH)_4$ .

Sample	$S_{BET}$ ( $m^2/g$ )	$V_T$ ( $cm^3/g$ )	$V_{meso}$ ( $cm^3/g$ )	$V_{meso}/V_T$
$Zr(OH)_4$	216	0.139	0.050	0.640
$Zr(OH)_4$ /GO Nanocomposite	274	0.262	0.251	0.958

The thermal and structural characteristics of  $Zr(OH)_4$ /GO nanocomposite and pristine  $Zr(OH)_4$  were determined by thermal characterization techniques with elevating temperature. The TGA curves of the materials are presented in Figure 3. Samples were pre-conditioned in the desiccator at ambient temperature for 24 h before TGA analysis. Both of materials showed gradual weight losses in the broad temperature range of 30–500 °C. The final weight loss at 800 °C of  $Zr(OH)_4$ /GO nanocomposite and pristine  $Zr(OH)_4$  were 14 and 26%, respectively, which were mainly attributed to removal of the physisorbed water and dehydroxylation [20,39]. It should be noted that the weight loss was obviously larger in pristine  $Zr(OH)_4$ , indicating that more water was adsorbed. These results could be attributed to variation of porosity of  $Zr(OH)_4$  due to the formation of nanocomposite of GO.

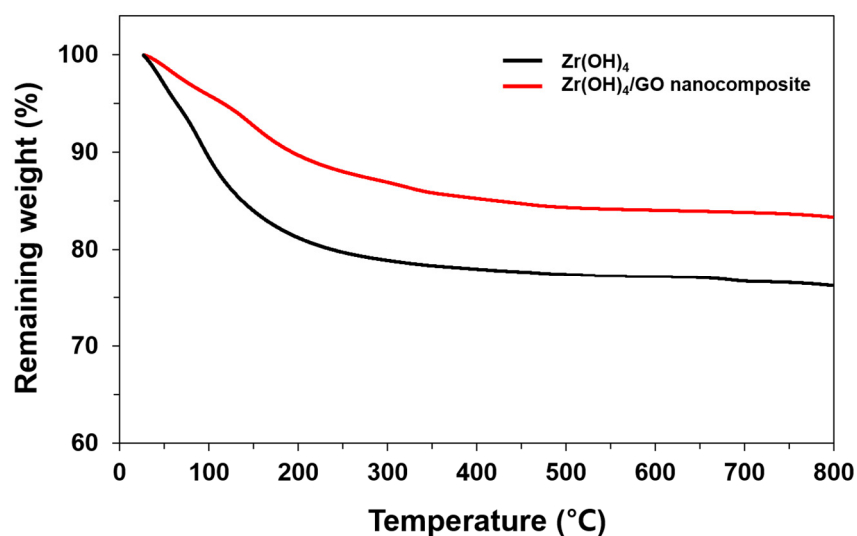


**Figure 3.** Profiles of thermogravimetric analysis (TGA) of Zr(OH)<sub>4</sub>/GO nanocomposite and pristine Zr(OH)<sub>4</sub>. The loss percentages of Zr(OH)<sub>4</sub>/GO nanocomposite and Zr(OH)<sub>4</sub> are 17% and 24%, respectively. All samples were heated at 30 to 800 °C with a heating rate of 5 °C/min under N<sub>2</sub> gas.

### 3.2. Hydrolytic Degradation of Soman (GD) by Zr(OH)<sub>4</sub>/GO Nanocomposite and Pristine in High Humidity

To investigate the effect of atmosphere moisture on the degradation of soman (GD) by Zr(OH)<sub>4</sub>/GO nanocomposite and pristine Zr(OH)<sub>4</sub>, the degradation experiments were carried out in the neat state at room temperature. The samples were pretreated for various times (72, 168, and 324 h) at 80% RH in a 25 °C convection oven. Figure 4 shows the degradation rate of soman (GD) on Zr(OH)<sub>4</sub>/GO nanocomposite and pristine Zr(OH)<sub>4</sub> during 10 min reaction time. It is worthy to note that Zr(OH)<sub>4</sub>/GO nanocomposite exhibited better performance for degrading soman (GD) even after 324 h exposure to high-humidity conditions. That is, Zr(OH)<sub>4</sub>/GO nanocomposite maintains a good degradation ability in neat condition whereas Zr(OH)<sub>4</sub> lost activity for soman (GD) when exposed to 80% RH condition for prolonged time (Figure S3).

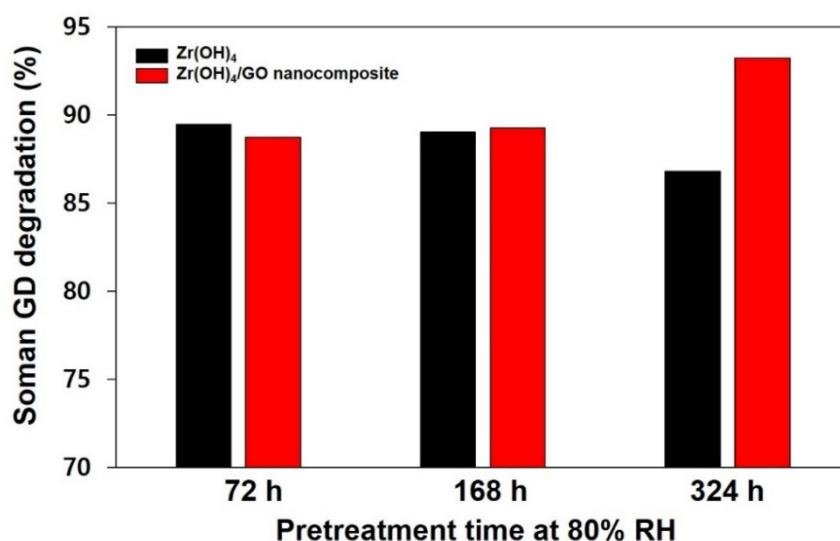


**Figure 4.** Degradation of nerve agent soman (GD) by and Zr(OH)<sub>4</sub>/GO nanocomposite and pristine Zr(OH)<sub>4</sub>. The samples were pretreated for various times (72, 168, 324 h) at 80% RH in a 25 °C convection oven.

To more clearly confirm the effect of water on the performance of  $Zr(OH)_4/GO$  nanocomposite reactive particles in the degradation reaction of soman (GD), the degradation experiments were performed in aqueous solution. The results, presented in Figure S4, show that the degradation rate of soman (GD) by  $Zr(OH)_4/GO$  nanocomposite in the aqueous solution seems to follow the catalytic reaction, similar to those obtained in previous study [14]. It is noted that the pH of the water containing  $Zr(OH)_4/GO$  nanocomposite is 8.57, which is the same as of pristine  $Zr(OH)_4$  solution. After reaction with soman (GD), however, the pH of  $Zr(OH)_4/GO$  nanocomposite solution decreased to 5.45, confirming the formation of acidic products, PMPA along with hydrogen fluoride (HF). Although some  $OH^-$  present by reaction of  $Zr(OH)_4/GO$  nanocomposite with the water may be the hydrolyzing agent for soman (GD), the results, presented in Figure 4 (along with Figure 5 discussed later) show that the hydrolysis is more directly due to  $Zr(OH)_4/GO$  nanocomposite rather than the pH itself of the aqueous solution.

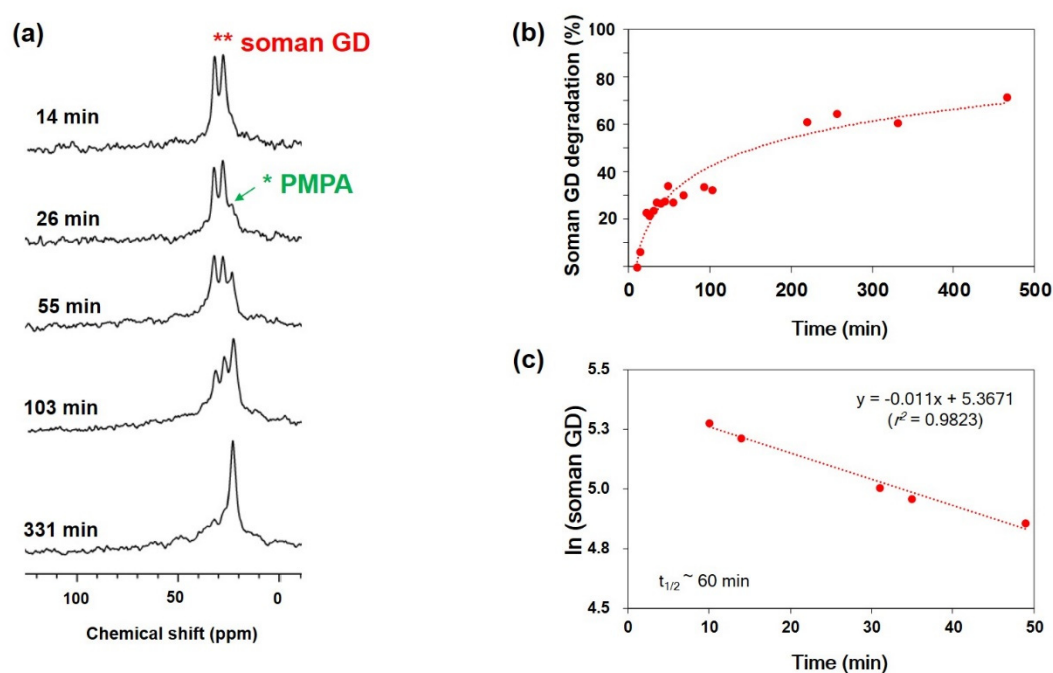


**Figure 5.** (a)  $^{31}P$  SS-MAS NMR spectra for the reaction mixture of  $Zr(OH)_4/GO$  nanocomposite and soman (GD), showing the presence of soman (GD) (27.3, 31.6 ppm) and PMPA (24.4 ppm), (b) reaction profile of catalytic degradation of soman (GD) upon exposure to  $Zr(OH)_4/GO$  nanocomposite in neat at 25 °C soman (GD): 5  $\mu$ L (0.028 mmol), sample weight: 93.8 mg, and (c) the plot of the soman (GD) agent loss in  $Zr(OH)_4/GO$  nanocomposite, showing linearity of the curve with following pseudo-first-order and an estimated half-life of 60 min.

Additionally,  $^{31}P$  SS-MAS NMR was used to determine the resulting reaction rates of soman (GD) on  $Zr(OH)_4/GO$  nanocomposite. As shown in Figure 5, over time, the sharp, twin peaks for soman (GD) at 27.3 and 31.6 ppm are replaced by a broad, single peak for PMPA near 24.4 ppm with its attendant spinning sidebands. The reaction profile shown in Figure 5b clearly shows the hydrolysis of soman (GD) by  $Zr(OH)_4/GO$  nanocomposite follows the catalytic reaction as shown in aqueous solution. That is, after a fast, initial reaction, and a steady state is achieved, exhibiting a first-order half-life of 60 min. By comparison, the half-lives observed for the soman (GD) reaction have been reported as 8.7 min by  $Zr(OH)_4$ , 28 min by  $MgO$ , and 270 min by  $CaO$ , each [18,40]. Catalytic turnover frequency (TOF) of  $Zr(OH)_4/GO$  nanocomposite in the solid state environment was estimated as  $0.0005 \text{ min}^{-1}$  by dividing the initial rate (in  $\text{mmole} \cdot \text{min}^{-1}$ ) by the catalyst loading (in  $\text{mmoles}$ ) [41]. Overall, the reaction of soman (GD) with  $Zr(OH)_4/GO$  nanocomposite is consistent with that previously reported for  $Zr(OH)_4$  and other solid hydrolysis catalysts [18,19]. From the above results in neat and



aqueous solutions, it can be seen that  $\text{Zr}(\text{OH})_4/\text{GO}$  nanocomposite, unlike  $\text{Zr}(\text{OH})_4$  itself, is suitable for decomposing nerve agents regardless of the air humidity conditions and even in the aqueous solution.

The degradation of soman (GD) is reportedly known to generate a nontoxic product, PMPA which has been shown to reside as surface-bound complexes [18,42,43]. The soman (GD) agent mainly degraded to PMPA upon reaction with  $\text{Zr}(\text{OH})_4/\text{GO}$  nanocomposite as well (Scheme 1, Figure 5 and S5). No further hydrolysis of PMPA to methylphosphonic acid (MPA) was observed during the 24 h observation period. Although soman (GD) can be hydrolyzed by surface hydroxyl groups and/or physisorbed water on the nanocomposite, we believe, the active hydroxyl sites are probably more available in  $\text{Zr}(\text{OH})_4/\text{GO}$  nanocomposite for the soman (GD) degradation.

### 3.3. Discussion of Water Adsorption Isotherms and DRIFT Spectra of $\text{Zr}(\text{OH})_4/\text{GO}$ Nanocomposite and Pristine $\text{Zr}(\text{OH})_4$

To investigate the reason for the differences in the soman (GD) agent hydrolysis of the materials in wet atmosphere conditions, water adsorption isotherms and DRIFT spectra were obtained for both  $\text{Zr}(\text{OH})_4/\text{GO}$  nanocomposite and pristine  $\text{Zr}(\text{OH})_4$ . First of all, water adsorption isotherms were obtained to examine the interaction between the materials and water. As shown in Figure 6,  $\text{Zr}(\text{OH})_4/\text{GO}$  nanocomposite exhibits type IV water isotherm, whereas  $\text{Zr}(\text{OH})_4$  shows type I water isotherm, as defined by International Union of Pure and Applied Chemistry (IUPAC) classification [16,44]. The type I water adsorption isotherm is characteristic of a hydrophilic material [14,45]. On the other hand, the type IV isotherm showing a sigmoidal course of an adsorption isotherm is usually observed the adsorption of water on hydrophobic porous materials such as aluminum phosphate, zeolite, metal–organic frameworks, and activated carbon [46]. Therefore, it could be speculated that the active sites of  $\text{Zr}(\text{OH})_4/\text{GO}$  nanocomposite are more available than those of  $\text{Zr}(\text{OH})_4$ , and, as a result, the soman (GD) interacts with more active sites, such that the soman (GD) hydrolysis ability of  $\text{Zr}(\text{OH})_4$  could be enhanced even under atmosphere water present at 80% RH.

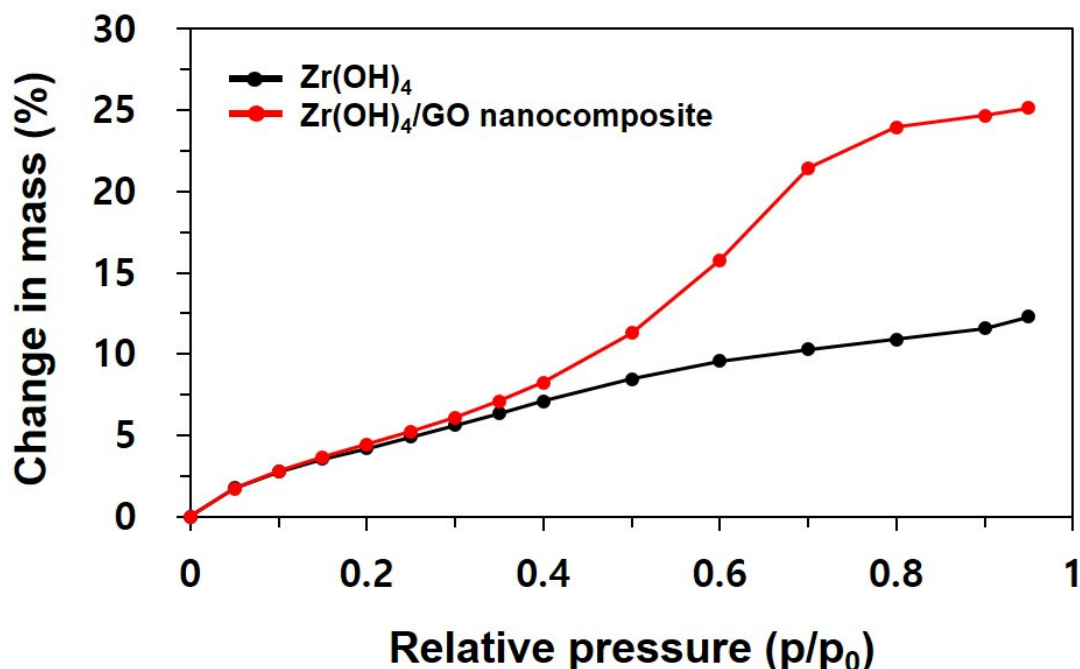
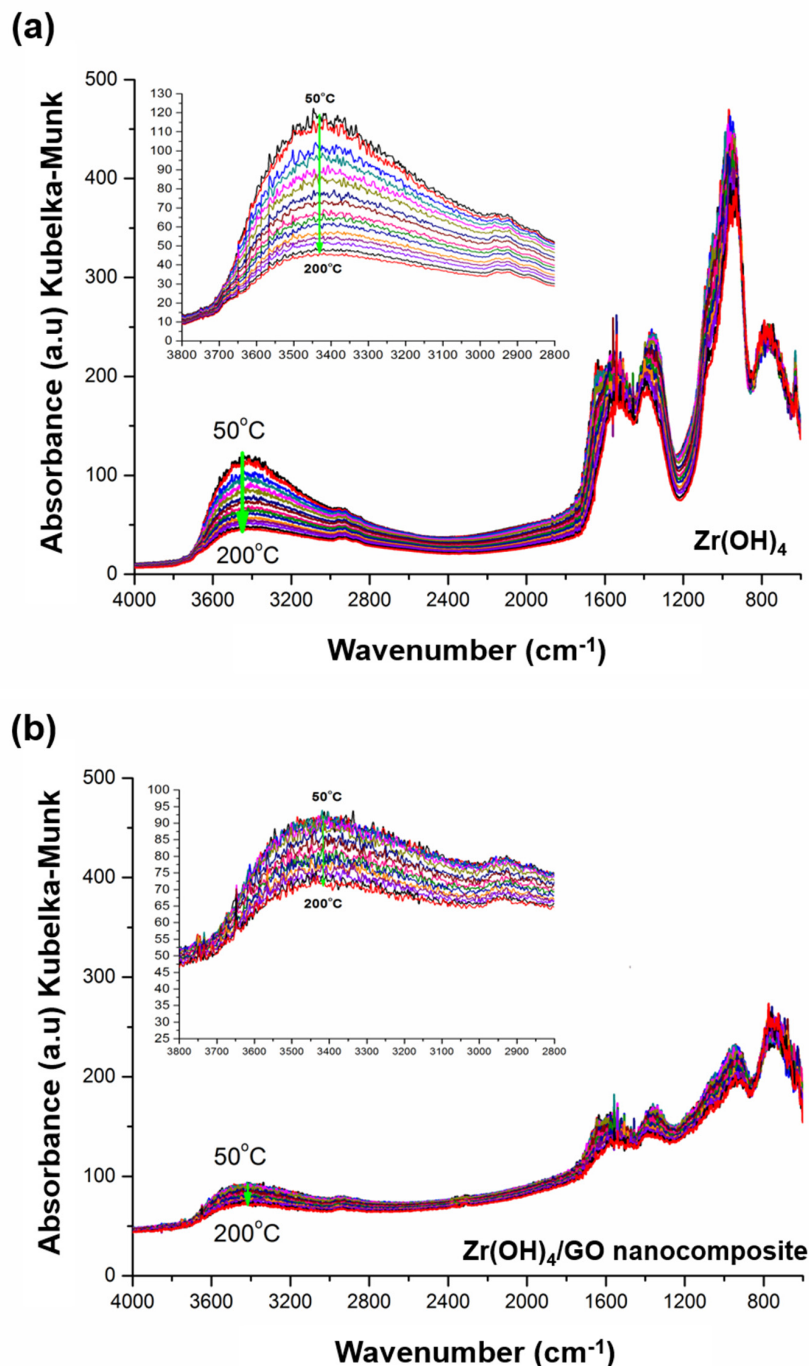


Figure 6. Water adsorption isotherms of  $\text{Zr}(\text{OH})_4/\text{GO}$  nanocomposite and pristine  $\text{Zr}(\text{OH})_4$  at 25 °C.

DRIFT spectra were obtained to more directly confirm the interaction between the materials and the adsorbed water. Both  $\text{Zr}(\text{OH})_4/\text{GO}$  nanocomposite and pristine,  $\text{Zr}(\text{OH})_4$  were pretreated at 25 °C and 80% RH in a convection oven overnight before the DRIFT measurements. The DRIFT spectra presented in Figure 7 show how the water adsorbed on the surface of the materials changes

with increasing temperature (from 50 to 200 °C). For both materials, the broad peaks from 2800 to 3600  $\text{cm}^{-1}$ , corresponding to the hydrogen-bonded water (adsorbed) stretching, decrease with increasing temperature by being desorbed. However, it is worth noting that the decrease of this band was considerably greater for pristine  $\text{Zr}(\text{OH})_4$  than for the  $\text{Zr}(\text{OH})_4/\text{GO}$  nanocomposite, indicating that the interaction between the material and the adsorbed water is weaker in  $\text{Zr}(\text{OH})_4/\text{GO}$  nanocomposite than that of  $\text{Zr}(\text{OH})_4$ . These results confirm that the more active sites such as the surface hydroxyl group are available for the degradation of soman (GD) in the case of  $\text{Zr}(\text{OH})_4/\text{GO}$  nanocomposite exposed to a humidity environment of 80% RH.



**Figure 7.** Time-resolved absorbance DRIFT spectra of (a)  $\text{Zr}(\text{OH})_4/\text{GO}$  nanocomposite and (b) pristine  $\text{Zr}(\text{OH})_4$ . The temperature of the sample cup for DRIFT increased from 50 to 200 °C at a rate of 10 °C/min and was held for 5 min after every 10 °C increase. Spectra were collected every 5 min.

It is worthy to note that GO in the composite with Zr(OH)<sub>4</sub> can make the pores less hydrophilic, and thus prevent water from blocking the free hydroxyl groups of the surface. We believe that in the case of Zr(OH)<sub>4</sub>/GO nanocomposite, the increase in mesoporous spaces and in hydrophobicity generated certain synergy, resulting in the better hydrolytic performance of soman (GD) after the long-term exposure to the high-humidity environment, such as 80% RH.

#### 4. Conclusions

Zr(OH)<sub>4</sub>/GO nanocomposite and pristine Zr(OH)<sub>4</sub> were prepared by a simple dropwise method. In particular, Zr(OH)<sub>4</sub>/GO nanocomposite demonstrated enhanced performance for the degradation of the soman (GD) agent after a long exposure under high-humidity air conditions. The characterization studies showed that GO are well-embedded in Zr(OH)<sub>4</sub>/GO nanocomposite, displaying a more porous structure and larger specific surface areas than pristine Zr(OH)<sub>4</sub>. Reaction profiles of Zr(OH)<sub>4</sub>/GO nanocomposite with soman (GD) show that after a fast initial reaction, a steady state is achieved exhibiting a first-order half-life of 60 min and TOF of 0.0005 min<sup>-1</sup>. The water adsorption and DRIFT data of Zr(OH)<sub>4</sub>/GO nanocomposite showed that the interaction between the materials and the adsorbed water was weaker in Zr(OH)<sub>4</sub>/GO nanocomposite, indicating that soman (GD) will have more access to the active sites in the high-humidity condition. With further optimization, the Zr(OH)<sub>4</sub>/GO nanocomposite has the potential to be used in the real world for decontamination application due to superior properties.

**Supplementary Materials:** The following are available online at <http://www.mdpi.com/1996-1944/13/13/2954/s1>, Figure S1: (a) SEM images and EDS spectral results of the elements C, O, Zr of Zr(OH)<sub>4</sub>/GO nanocomposite (b) Spot 1, (c) Spot 2, Figure S2: XRD patterns for pristine Zr(OH)<sub>4</sub> and Zr(OH)<sub>4</sub>/GO nanocomposite. XRD patterns were obtained from 10° to 70°, indicating that there is no change in Zr(OH)<sub>4</sub> structure by forming nanocomposite with GO, Figure S3: (a) GC of remaining soman (GD) after reaction with Zr(OH)<sub>4</sub>/GO nanocomposite and Zr(OH)<sub>4</sub>, each under 80% RH pretreatment for 324 h. GC spectrum of soman (GD) itself was inserted for comparison, (b) enlarged spectra of GC in (a) for clarity, Figure S4: Comparison of hydrolytic degradation of the nerve agent, soman (GD) by exposure to Zr(OH)<sub>4</sub>/GO nanocomposite and pristine Zr(OH)<sub>4</sub> in the water at ambient temperature, Figure S5: (a) GC spectra of soman (GD) standard ( $R_t = 11.7, 11.8$  min) and PMPA-TMS ( $R_t = 15.9$  min). Mass spectra of (b) soman (GD) and (c) PMPA-TMS. Note the characteristic fragment ion peaks were seen:  $m/z = 99.0, 126.1$  for GD and  $m/z = 153.0, 169.1$  for PMPA-TMS.

**Author Contributions:** Conceptualization, Y.J. and S.J.; data curation, S.J., D.K. and M.-K.K., and H.J. (Heesoo Jung); formal analysis, Y.J., S.J., D.K., H.J. (Hyunsook Jung), and M.-K.K.; investigation, S.J., D.K., Y.J., and M.-K.K.; project administration, H.J. (Hyunsook Jung), and Y.J.; writing—original draft Y.J. and S.J.; writing—review and editing, Hy.J., S.J., Y.J., D.K., and He.J. All authors have read and agreed to the published version of the manuscript.

**Funding:** This research received no external funding

**Acknowledgments:** The authors gratefully acknowledge the provision of the soman (GD) agent by the Chemical Analysis Test and Research Lab. We thank Mihyun Kim for assisting XRD and SEM analyses.

**Conflicts of Interest:** The authors report no potential conflict of interest.

#### References

1. Barba-Bon, A.; Martinez-Manez, R.; Sancenon, F.; Costero, A.M.; Gil, S.; Perez-Pla, F.; Llopis, E. Towards the design of organocatalysts for nerve agents remediation: The case of the active hydrolysis of DCNP (a Tabun mimic) catalyzed by simple amine-containing derivatives. *J. Hazard Mater.* **2015**, *298*, 73–82. [[CrossRef](#)] [[PubMed](#)]
2. Mohammad, M.; Emadodin, D.; Darchini, M.; Mahdi, B.M. Advances in toxicology and medical treatment of chemical warfare nerve agents. *DARU J. Pharm. Sci.* **2012**, *20*, 81.
3. Organization for the Prohibition of Chemical Weapons Convention on the Prohibition of the Development, Production, Stockpiling and Use of Chemical Weapons and on Their Destruction. Available online: <https://www.opcw.org/chemical-weapons-convention> (accessed on 27 September 2005).
4. Picard, B.; Chataigner, I.; Maddaluno, J.; Legros, J. Introduction to chemical warfare agents, relevant simulants and modern neutralisation methods. *Org. Biomol. Chem.* **2019**, *17*, 6528–6537. [[CrossRef](#)] [[PubMed](#)]

5. Jang, Y.J.; Kim, K.; Tsay, O.G.; Atwood, D.A.; Churchill, D.G. Update 1 of: Destruction and Detection of Chemical Warfare Agents. *Chem. Rev.* **2015**, *115*, PR1–PR76. [[CrossRef](#)] [[PubMed](#)]
6. Yang, Y.C.; Baker, J.A.; Ward, J.R. Decontamination of chemical warfare agents. *Chem. Rev.* **1992**, *92*, 1729–1743. [[CrossRef](#)]
7. Wagner, G.W.; Sorrick, D.C.; Procell Brickhouse, M.D.; Mcvey, I.F.; Schwartz, L.I. Decontamination of VX, GD, and HD on a surface using modified vaporized hydrogen peroxide. *Langmuir* **2007**, *23*, 1178–1186. [[CrossRef](#)] [[PubMed](#)]
8. Ryu, S.G.; Lee, H.W. Effectiveness and reaction networks of H<sub>2</sub>O<sub>2</sub> vapor with NH<sub>3</sub> gas for decontamination of the toxic warfare nerve agent, VX on solid surface. *J. Environ. Sci. Health Part A* **2015**, *50*, 1417–1427.
9. Sciniciz, L. History of chemical and biological warfare agents. *Toxicology* **2005**, *214*, 167–181. [[CrossRef](#)]
10. Liu, Y.; Moon, S.Y.; Hupp, J.T.; Farha, O.K. Dual-function metal-organic framework as a versatile catalyst for detoxifying chemical warfare agent simulants. *ACS Nano* **2015**, *9*, 12358–12364. [[CrossRef](#)]
11. Seredych, M.; Bandoz, T.J. Effects of surface features on adsorption of SO<sub>2</sub> on graphite oxide/Zr(OH)<sub>4</sub> composites. *J. Phys. Chem. C* **2010**, *114*, 14552–14560. [[CrossRef](#)]
12. Seredych, M.; Bandoz, T.J. Reactive adsorption of hydrogen sulfide on graphite oxide/Zr(OH)<sub>4</sub> composites. *Composites Chem. Eng. J.* **2011**, *166*, 1032–1038. [[CrossRef](#)]
13. Chanvan, S.; Vitillo, J.G.; Gianolio, D.; Zavorotynska, O.; Civalleri, B.; Jakobsen, S.; Nilsen, M.H.; Valenzano, L.; Lamberti, C.; Lillerud, K.P.; et al. H<sub>2</sub> storage in isostructural UiO-67 and UiO-66 MOFs. *Phys. Chem. Chem. Phys.* **2012**, *14*, 1614–1626. [[CrossRef](#)] [[PubMed](#)]
14. Ryu, S.G.; Kim, M.K.; Park, M.K.; Jang, S.O.; Kim, S.H.; Jung, H.S. Availability of Zr-based MOFs for the degradation of nerve agents in all humidity conditions. *Micropor. Mesopor. Mat.* **2019**, *274*, 9–16. [[CrossRef](#)]
15. Kandiah, M.; Nilsen, M.H.; Usseglio, S.; Jakobsen, S.; Olsbye, U.; Tilset, M.; Larabi, C.; Quadrelli, E.A.; Bonino, F.; Lillerud, K.P. Synthesis and stability of tagged UiO-66 Zr-MOFs. *Chem. Mater.* **2010**, *22*, 6632–6640. [[CrossRef](#)]
16. Zheng, Y.; Zheng, S.; Xue, H.; Pang, H. Metal-organic framework/graphene-based materials: Preparations and applications. *Adv. Funct. Mater.* **2018**, *28*, 1804950. [[CrossRef](#)]
17. Balow, R.B.; Lundin, J.G.; Daniels, G.C.; Gordon, W.O.; McEntee, M.; Peterson, G.W.; Wynne, J.H.; Pehrsson, P.E. Environmental effects on zirconium hydroxide nanoparticles and chemical warfare agent decomposition: Implications of atmospheric water and carbon dioxide. *ACS Appl. Mater. Interfaces* **2017**, *9*, 39747–39757. [[CrossRef](#)]
18. Bandoz, T.J.; Laskoski, M.; Mahle, J.; Mogilevsky, G.; Peterson, G.W.; Rossin, J.A.; Wagner, G.W. Reactions of VX, GD, and HD with Zr(OH)<sub>4</sub>: Near instantaneous decontamination of VX. *J. Phys. Chem. C* **2012**, *116*, 11606–11614. [[CrossRef](#)]
19. Wagner, G.W.; Peterson, G.W.; Mahle, J.J. Effects of adsorbed water and surface hydroxyls on the hydrolysis of VX, GD, and HD on titania materials: The development of self-decontaminating paints. *Ind. Eng. Chem. Res.* **2012**, *51*, 3598–3603. [[CrossRef](#)]
20. Giannakoudakis, D.A.; Mitchell, J.K.; Bandoz, T.J. Reactive adsorption of mustard gas surrogate on zirconium (hydr)oxide/graphite oxide composites: The role of surface and chemical features. *J. Mater. Chem. A* **2016**, *4*, 1008–1019. [[CrossRef](#)]
21. Peterson, G.W.; Wagner, G.W.; Keller, J.H.; Rossin, J.A. Enhanced cyanogen chloride removal by the reactive zirconium hydroxide substrate. *Ind. Eng. Chem. Res.* **2010**, *49*, 11182–11187. [[CrossRef](#)]
22. Peterson, G.W.; Rossin, J.A. Removal of chlorine gases from streams of air using reactive zirconium hydroxide based filtration media. *Ind. Eng. Chem. Res.* **2012**, *51*, 2675–2681. [[CrossRef](#)]
23. Colon-Ortiz, J.; Landers, J.M.; Gordon, W.O.; Abalboa, A.; Karwacki, C.J.; Neimark, A.V. Disordered mesoporous zirconium (hydr)oxides for decomposition of dimethyl chlorophosphate. *ACS Appl. Mater. Interfaces* **2012**, *11*, 17931–17939. [[CrossRef](#)] [[PubMed](#)]
24. Jeon, S.M.; Balow, R.B.; Daniels, G.C.; Ko, J.S.; Pehrsson, P.E. Conformal nanoscale zirconium hydroxide films for decomposing chemical warfare agents. *ACS App. Nano Mater.* **2019**, *2*, 2295–2307. [[CrossRef](#)]
25. Das, R.S.; Warkhade, S.K.; Kumar, A.; Wankhade, A.V. Graphene oxide-based zirconium oxide nanocomposite for enhanced visible light-driven photocatalytic activity. *Res. Chem. Intermediat.* **2019**, *45*, 1689–1705. [[CrossRef](#)]
26. Wang, H.L.; Casalongue, H.S.; Liang, Y.Y.; Liang, H.J.; Dai, H.J. Ni(OH)<sub>2</sub> Nanoplates Grown on Graphene as Advanced Electrochemical Pseudocapacitor Materials. *J. Am. Chem. Soc.* **2010**, *132*, 7472–7477. [[CrossRef](#)]

27. Tang, J.; Wang, J. Fe-based metal organic framework/graphene oxide composite as an efficient catalyst for Fento-like degradation of methyl orange. *RSC Adv.* **2017**, *7*, 50829–50837. [[CrossRef](#)]
28. Zhang, G.; Li, G.; Lu, H.; Lv, Q.; Sun, Z.G. Synthesis, characterization and photocatalytic properties of MIL-53(Fe)-graphene hybrid materials. *RSC Adv.* **2014**, *15*, 7594–7600. [[CrossRef](#)]
29. Petit, C.; Bandoz, T.J. MOF-Graphite Oxide Composites: Combining the Uniqueness of Graphene Layers and Metal-Organic Frameworks. *Adv. Mater.* **2009**, *21*, 4753–4757. [[CrossRef](#)]
30. Zubir, N.A.; Yacou, C.; Motuzas, J.; Zhang, X.W.; Zhao, X.S.; da Costa, J.C.D. The sacrificial role of graphene oxide in stabilizing a Fenton-like catalyst GO-Fe<sub>3</sub>O<sub>4</sub>. *Chem. Commun.* **2015**, *45*, 9291–9293. [[CrossRef](#)]
31. Jung, H.S.; Lim, K.C. Fate and degradation of the chemical warfare agent soman on sands. *Environ. Chem. Lett.* **2016**, *14*, 367–372. [[CrossRef](#)]
32. Yokota, T.; Hiraga, K.; Yamane, H.; Takai-Iashi, N. Mass spectrometry of trimethylsilyl derivatives of gibberellin glucosides and glucosyl ester. *Phytochemistry* **1975**, *14*, 1569–1574. [[CrossRef](#)]
33. ALOthman, Z.A. A Review: Fundamental Aspects of Silicate Mesoporous Materials. *Materials* **2012**, *5*, 2874–2902. [[CrossRef](#)]
34. Boer, J.H.D.; Lippens, B.C.; Lisen, B.G.; Broekhoff, J.C.P.; Heuvel, A.V.D.; Osinga, T.J. Thet-curve of multimolecular N<sub>2</sub>-adsorption. *J. Colloid Interf. Sci.* **1966**, *21*, 405–414. [[CrossRef](#)]
35. Wu, Z.; Zhu, H.; Yuan, X.; Wang, H.; Wang, L.; Chen, X.; Zeng, G.; Wu, Y. Adsorptive removal of methylene blue by rhamnolipid-functionalized graphene oxide from wastewater. *Water Res.* **2014**, *67*, 330–344. [[CrossRef](#)]
36. Vellingiri, K.; Philip, L.; Kim, K.H. Metal-organic frameworks as media for the catalytic degradation of chemical warfare agents. *Coord. Chem. Rev.* **2017**, *353*, 159–179. [[CrossRef](#)]
37. Matito-Martos, I.; Moghadam, P.Z.; Li, A.; Colombo, V.; Navarro, J.A.R.; Calero, S.; Fairen-Jimenez, D. Discovery of an Optimal Porous Crystalline Materials for the Capture of Chemical Warfare Agents. *Chem. Mater.* **2018**, *30*, 4571–4579. [[CrossRef](#)]
38. Koning, M.C.D.; Grol, M.V.; Breijaert, T. Degradation of Paraoxon and the Chemical Warfare Agents VX, Tabun, and Soman by the Metal-Organic Frameworks UiO-66-NH<sub>2</sub>, MOF-808, NU-1000, and PCN-777. *Inorg. Chem.* **2017**, *56*, 11804–11809. [[CrossRef](#)]
39. Peterson, G.W.; Rossin, J.A.; Karwacki, C.J.; Glover, T.G. Surface chemistry and morphology of zirconia polymorphs and the influence on sulfur dioxide removal. *J. Phys. Chem. C* **2011**, *115*, 9644–9650. [[CrossRef](#)]
40. Wagner, G.W.; Bartram, P.W.; Koper, O.; Klabunde, K.J. Reactions of VX, GD, and HD with nanosize MgO. *J. Phys. Chem. B* **1999**, *103*, 3225–3228. [[CrossRef](#)]
41. Katz, M.J.; Klet, R.C.; Moon, S.-Y.; Mondloch, J.E.; Hupp, J.T.; Farha, O.K. One step backward is two steps forward: Enhancing the hydrolysis rate of UiO-66 by decreasing [OH<sup>-</sup>]. *ACS Catal.* **2015**, *5*, 4637–4642. [[CrossRef](#)]
42. Wagner, G.W.; Procell, L.R.; O'Connor, R.J.; Munavalli, S.; Carnes, C.L.; Kapoor, P.N.; Klabunde, K.J. Reactions of VX, GB, GD, and HD with nanosize Al<sub>2</sub>O<sub>3</sub>. Formation of aluminophosphonates. *J. Am. Chem. Soc.* **2001**, *123*, 1636–1644. [[CrossRef](#)] [[PubMed](#)]
43. Wagner, G.W.; Procell, L.R.; Munavalli, S. <sup>27</sup>Al, <sup>47,49</sup>Ti, <sup>31</sup>P, and <sup>13</sup>C MAS study of VX, GD, and HD reactions with nanosize Al<sub>2</sub>O<sub>3</sub>, conventional Al<sub>2</sub>O<sub>3</sub> and TiO<sub>2</sub>, and aluminium and titanium metal. *J. Phys. Chem. C* **2007**, *111*, 17564–17569. [[CrossRef](#)]
44. Bale, S.; Samanidou, V.; Deliyanni, E. Effect of the reduction degree of graphene oxide on the adsorption of Bisphenol A. *Chem. Eng. Res. And Des.* **2016**, *109*, 573–585. [[CrossRef](#)]
45. Roy, A.; Srivastavana, A.K.; Singh, B.; Mahato, T.H.; Shah, D.; Halve, A.K. Degradation of sulfur mustard and 2-chloroethyl sulfide on Cu-BTC metal-organic framework. *Micropor. Mesopor. Mater.* **2012**, *162*, 207–212. [[CrossRef](#)]
46. Buttersack, C. Modeling of type IV and V sigmoidal adsorption isotherms. *Phys. Chem. Chem. Phys.* **2019**, *21*, 5614–5626. [[CrossRef](#)]

